Luminosities and Masses of Single Galactic Post-asymptotic Giant Branch Stars with Distances from Gaia EDR3: The Revelation of an *s*-process Diversity

Devika Kamath[1,2] , Hans Van Winckel[3] , Paolo Ventura[4] , Maksym Mohorian[1,2] , Bruce J. Hrivnak[5] ,
Flavia Dell'Agli[4] , and Amanda Karakas[6,7]

[1] Department of Physics and Astronomy, Macquarie University, Sydney, NSW, Australia; devika.kamath@mq.edu.au
[2] Astronomy, Astrophysics and Astrophotonics Research Centre, Macquarie University, Sydney, NSW, Australia
[3] Instituut voor Sterrenkunde, K.U.Leuven, Celestijnenlaan 200D bus 2401, B-3001, Leuven, Belgium
[4] INAF, Observatory of Rome, Via Frascati 33, I-00077 Monte Porzio Catone (RM), Italy
[5] Department of Physics and Astronomy, Valparaiso University, Valparaiso, IN 46383, USA
[6] School of Physics & Astronomy, Monash University, Clayton VIC 3800, Australia
[7] ARC Centre of Excellence for All Sky Astrophysics in 3 Dimensions (ASTRO 3D), Australia

Abstract

Post-asymptotic giant branch (AGB) stars are exquisite probes of AGB nucleosynthesis. However, the previous lack of accurate distances jeopardized comparison with theoretical AGB models. The Gaia Early Data Release 3 (Gaia EDR3) has now allowed for a breakthrough in this research landscape. In this study, we focus on a sample of single Galactic post-AGBs for which chemical abundance studies were completed. We combined photometry with geometric distances to carry out a spectral energy distribution (SED) analysis and derive accurate luminosities. We subsequently determined their positions on the Hertzsprung-Russell (HR) diagram and compared this with theoretical post-AGB evolutionary tracks. While most objects are in the post-AGB phase of evolution, we found a subset of low-luminosity objects that are likely to be in the post-horizontal branch phase of evolution, similar to AGB-manqué objects found in globular clusters. Additionally, we also investigated the observed bimodality in the *s*-process enrichment of Galactic post-AGB single stars of similar $T_{\rm eff}$ and metallicities. This bimodality was expected to be a direct consequence of luminosity with the *s*-process rich objects having evolved further on the AGB. However, we find that the two populations, the *s*-process enriched and non-enriched, have similar luminosities (and hence initial masses), revealing an intriguing chemical diversity. For a given initial mass and metallicity, AGB nucleosynthesis appears inhomogeneous and sensitive to other factors, which could be mass loss, along with convective and non-convective mixing mechanisms. Modeling individual objects in detail will be needed to investigate which parameters and processes dominate the photospheric chemical enrichment in these stars.

Unified Astronomy Thesaurus concepts: Post-asymptotic giant branch stars (2121); Galaxy abundances (574); Chemical abundances (224); Asymptotic giant branch (108); S-process (1419); Nucleosynthesis (1131); Spectral energy distribution (2129); Photometry (1234); Stellar luminosities (1609); Stellar properties (1624); Dredge-up (409); Late stellar evolution (911)

1. Introduction

Low- and intermediate-mass (LIM) stars (1–8 $M_{\odot}$) stars in their asymptotic giant branch (AGB) phase of evolution are estimated to produce ∼90% of the solid material injected into the interstellar medium (Sloan et al. 2008) and are known to be one of the major producers of elements such as carbon and nitrogen and about half of the elements heavier than iron (Kobayashi et al. 2020). AGB stars are clearly key contributors to the chemical enrichment of the universe. Traditionally, AGB stars are popularly used as tracers to quantify elemental isotopes (e.g., García-Hernández et al. 2007; Hinkle et al. 2016). However, they pose many challenges for tracing AGB nucleosynthesis because their spectra are veiled by molecular lines (Abia et al. 2008), and modeling of their dynamical atmospheres is rather complex and uncertain (Pérez-Mesa et al. 2019).

In the evolution of LIM stars, post-asymptotic giant branch (post-AGB) objects are considered to be those in transition between the AGB and the planetary nebula (PN) phase (see Van Winckel 2003a, for a review). Post-AGB stars are typically of A−K spectral types, with a characteristic mid-IR excess, indicative of their dusty circumstellar environment. At the very end of the AGB phase, stars lose mass via a powerful wind, driven by stellar pulsations (Vassiliadis & Wood 1993) or by interaction with another star for stars in binary systems (Nie et al. 2012; Kamath et al. 2016). When the stellar envelope is reduced to a few hundredths of a solar mass, the post-AGB evolutionary phase starts (e.g., Miller Bertolami 2016). Depending on the opacity of the circumstellar shell, the central star becomes exposed. Given their effective temperature, the photospheric spectra are dominated by atomic transitions, making post-AGB stars exquisite probes to examine the elements produced by the star during and prior to the AGB phase (e.g., De Smedt et al. 2012, 2016, and references therein). Additionally, objects in the post-AGB phase (as shown in the spectral energy distributions, SEDs, presented in Figure 2) allow for full characterization of the central star as well as the circumstellar material. The systematic identification

and study of post-AGB stars began with the IRAS satellite ~30 yr ago (Kwok et al. 1987). Currently, the known samples of post-AGB stars are those residing in the galaxy and the Magellanic Clouds (MCs). The Toruń catalog (Szczerba et al. 2007) lists around 391 likely optically visible post-AGB candidates in the galaxy, while systematic photometric and spectroscopic studies (van Aarle et al. 2011; Kamath et al. 2014, 2015) have provided catalogs of spectroscopically verified, optically visible post-AGB candidates in the Magellanic Clouds (MCs).

Observational studies of the known sample of post-AGB stars in the galaxy and the MCs have shown their SEDs can provide critical clues on the likely single or binary nature of these objects (see Van Winckel et al. 2009; Kamath et al. 2015; Oomen et al. 2018, and references therein). Single post-AGBs (referred to as "shell-sources") show a distinct double-peaked SED, where the peak at optical wavelengths is representative of the central post-AGB star and the peak at infrared (IR) wavelengths is indicative of the detached dusty circumstellar envelope. The binary objects (referred to as "disk sources") show a broad onset in the near-IR, indicative of hot circumstellar dust that resides in a circumbinary disk around the post-AGB binary system (see van Winckel 2017 and references therein).

The single or binary nature also has a significant effect on the observed photospheric abundances. As expected, many single post-AGB stars show signatures of AGB nucleosynthesis, such as enhancements of carbon (C), nitrogen (N), oxygen (O), and s-process elements[8] (e.g., De Smedt et al. 2012, 2016). For post-AGB stars in binary systems, the circumbinary disk has been shown to play a key role in altering the photospheric chemistry, resulting in a "depleted" chemical pattern, wherein the stellar photosphere is depleted in refractory elements (e.g., Oomen et al. 2018; Kamath & Van Winckel 2019).

In addition to the above-mentioned chemical patterns, post-AGB stars also show intriguing chemical diversities (Van Winckel 2003a; Kamath 2020). For instance, the study by Van Winckel (2003b) reported a subset of single Galactic post-AGB stars that show no signatures of s-process enhancements (referred to as "have-nots"). Also, in our previous study (Kamath et al. 2017), we reported a subset of luminous single post-AGB stars (one in the SMC and two in the galaxy) that showed neither traces of carbon enhancements nor of s-process elements and are likely to have failed the third dredge-up. These chemical diversities directly point to the complex and poorly understood chemical mixing and nucleosynthesis that occurs during and prior to the AGB phase of evolution in these stars.

In this study, we focus on the observed bimodality in the enrichment of s-process elements, first reported by Van Winckel (2003b) almost two decades ago, based on detailed chemical abundance studies of 17 single post-AGB stars in the galaxy. In Van Winckel (2003b) the two groups of objects were referred to as "haves"— those with significant s-process enrichment and "have-nots", i.e., those without traces of s-process enhancements. It was noted that both the "haves" and "have-nots" were of similar effective temperatures and metallicities ([Fe/H]). Whether the bimodality reflected a true distribution due to intrinsic AGB nucleosynthesis (which is highly dependent on initial mass and metallicity) or whether it

was due to an observational bias in the selection criteria of well-studied post-AGB stars remained unsolved.

The challenges in solving this chemical bimodality have been two-fold. First, owing to the brevity of this phase (<10,000 yr depending on metallicity; Miller Bertolami 2016), post-AGB stars are relatively rare, and finding sufficient numbers of them is difficult. Second, element production depends upon the initial mass and composition of the star. So far, poorly known distances to stars in our galaxy stymied the determination of accurate luminosities and initial masses to these objects. In this study, we exploit the early release of Gaia EDR3 data, which has provided the opportunity to obtain distances and hence luminosities to the sample of known single post-AGB stars in our galaxy. By comparing the position in the HR diagram with evolutionary tracks, we can estimate the initial masses, and finally, investigate the intriguing s-process enrichment bimodality observed in the single post-AGB stars in the galaxy.

2. Sample of Galactic Post-AGB Single Stars

For this study, we include all optically visible single post-AGB stars that were classified as "haves" (hereafter referred to as "s-process enriched") and "have-nots" (hereafter referred to as "non-s-process enriched") in Van Winckel (2003a, 2003b). Additionally, we also include more recently studied single post-AGB objects in the galaxy for which a reliable chemical abundance study has been carried out. The final sample of objects (see Table 1) comprises 18 s-process enriched objects and 13 non-s-process enriched objects. For convenience, Table 1 provides not only the object name but also a corresponding index with which we will refer to individual objects throughout the paper. We note that in Table 1 we have provided the most commonly used name for the object. For completeness, we have compiled all other names (e.g., IRAS names, HR names, HD names, SAO names, etc.) in Table 2 (see Appendix A). Additionally, in Figure 1 we show the distribution of the sample set (as a function of initial metallicity) in the galaxy. The objects are field stars and distributed along the Galactic disk. The relevant chemical abundances taken from the literature for each of the individual objects are listed in Table 3 of Appendix A.

We note that all the objects in our sample are likely either single stars or stars with undetermined wide orbits such that the binary interaction during evolution is limited and they likely evolve as single stars. All objects show the characteristic mid-IR excesses due to their circumstellar dust shells and expanding molecular envelopes (as mentioned in Section 1). This is evidenced by their double-peaked SED (see Appendix B). A few objects without detected dust (e.g., Object 22: HD 107369, Object 25: HR 6144, Object 31: HR 7671) are high-latitude supergiants, also recognized to be in their post-AGB phase of evolution (e.g., Van Winckel 1997; Giridhar & Arellano Ferro 2005; Reyniers & Cuypers 2005). Additionally, photometric monitoring of the majority of these objects has revealed low-amplitude pulsations, with periods of 25–165 days for those with spectral types of G, F, A, and much shorter ones for the B stars (Hrivnak et al. 2010, 2015, 2021).

The majority of the northern objects have also been a part of systematic long-term radial velocity monitoring programs started in 2009 with the KU Leuven HERMES spectrograph (Raskin et al. 2011) on the 1.2 m Mercator telescope at the Roque de los Muchachos observatory and or by the long-term radial velocity monitoring program at the

---

[8] s-process elements are those created via the slow neutron-capture nucleosynthesis (see Gallino et al. 1998; Karakas & Lattanzio 2014, and references therein.)

Table 1
Fundamental Properties of the *s*-process-rich and Non-enriched Single Galactic Post-AGB Stars

Index	Object	Parallax (mas)	Error (mas)	RUWE	$z_{(1/\text{parallax})}$ (pc)	z_{BJ} (pc)	z_{BJL} (pc)	z_{BJU} (pc)	T_{eff} (K)	log g (dex)	E($B-V$)	$L/L_\odot$	$L_{\text{Lower}}/L_\odot$	$L_{\text{Upper}}/L_\odot$	Flag
						Post-AGB stars with *s*-process enrichment									
1	IRAS Z02229+6208	0.38	0.06	2.5	2627.53	2352.18	2063.48	2687.03	5952 ± 250	0.00	$1.90^{+0.08}_{-0.42}$	12959	9973	16911	Q2
2	IRAS 04296+3429	−0.38	0.17	5.8	−2635.11	5048.41	3899.38	7150.92	7272 ± 250	0.73	$2.03^{+0.06}_{-0.19}$	10009	5971	20082	Q2
3	IRAS 05113+1347	−0.01	0.15	6.7	−108371.7	4629.82	3312.65	8416.2	5025 ± 250	0.01	$0.75^{+0.35}_{-0.09}$	2037	1043	6731	Q2
4	IRAS 05341+0852	0.51	0.19	13.0	1960.07	2057.38	1603.89	2778.95	6274 ± 250	0.84	$1.18^{+0.19}_{-0.06}$	324	197	592	Q2
5	IRAS 06530−0213	0.24	0.07	3.7	4145.93	3777.67	2886.46	4990.04	7809 ± 250	1.70	$1.85^{+0.02}_{-0.18}$	4687	2736	8178	Q2
6	IRAS 07134+1005	0.45	0.02	0.9	2203.76	2099.09	1991.41	2209.25	7485 ± 250	0.50	$0.43^{+0.10}_{-0.09}$	5505	4955	6098	Q1
7	IRAS 07430+1115	3.06	0.5	21.8	327.04	360.93	299.59	442.65	5519 ± 250	1.43	$1.04^{+0.38}_{-0.12}$	20	14	30	Q2
8	IRAS 08143−4406	0.24	0.02	1.4	4198.54	4154.69	3877.12	4568.46	7013 ± 250	1.31	$1.53^{+0.95}_{-0.04}$	4509	3927	5452	Q1
9	IRAS 08281−4850	−0.14	0.07	6.0	−7300.68	11452.58	8728.27	15113.73	7462 ± 250	1.04	$1.23^{+0.11}_{-0.22}$	9584	5567	16692	Q2
10	IRAS 12360−5740	0.09	0.01	1.1	10970.73	9082.07	8261.41	10230.48	7273 ± 250	1.59	$1.01^{+0.35}_{-0.04}$	6258	5178	7940	Q1
11	IRAS 13245−5036	0.01	0.02	1.6	85919.8	14207.28	11305.73	17383.96	9037 ± 250	3.20	$0.64^{+0.14}_{-0.09}$	11221	7106	16800	Q2
12	IRAS 14325−6428	0.19	0.04	2.2	5220.46	4883.39	4261.63	5811.07	7256 ± 250	1.00	$1.07^{+0.22}_{-0.17}$	4935	3758	6988	Q2
13	IRAS 14429−4539	−0.11	0.51	2.8	−9372.15	3847.71	2160.1	6548.2	9579 ± 250	2.48	$2.63^{+0.36}_{-0.51}$	5049	1591	14624	Q2
14	IRAS 19500−1709	0.4	0.03	1.0	2504.9	2310.24	2164.96	2481.49	8239 ± 250	1.08	$0.56^{+0.03}_{-0.07}$	7053	6194	8138	Q1
15	IRAS 20000+3239	0.2	0.05	2.2	4880.07	4581.29	3695.53	6075.01	5478 ± 250	0.13	$1.76^{+0.09}_{-0.46}$	14342	9332	25218	Q2
16	IRAS 22223+4327	0.33	0.03	1.7	3007.27	2678.03	2546.9	2878.56	6008 ± 250	1.05	$0.43^{+0.28}_{-0.06}$	2163	1956	2499	Q2
17	IRAS 22272+5435	0.69	0.03	1.2	1457.75	1409.84	1355.87	1464.67	5325 ± 250	0.77	$0.88^{+0.34}_{-0.08}$	5659	5234	6108	Q1
18	IRAS 23304+6147	0.24	0.03	1.6	4226.42	3979.67	3620.05	4390.37	6276 ± 250	0.78	$1.83^{+0.17}_{-0.20}$	7712	6381	9386	Q2
						Post-AGB stars without *s*-process enrichment									
19	IRAS 01259+6823	0.62	0.14	1.3	1624.61	1781.38	1434.96	2456.33	5510 ± 250	2.50	$1.02^{+0.24}_{-0.07}$	340	220	646	Q1
20	IRAS 08187−1905	0.29	0.03	1.7	3473.16	3258.96	2917.24	3649.91	5772 ± 250	0.98	$0.07^{+0.31}_{-0.05}$	2619	2099	3286	Q2
21	SAO 239853	−0.01	0.07	3.7	−117255.41	8691.08	6485.52	12490.93	7452 ± 250	1.49	$0.30^{+0.08}_{-0.08}$	23490	13080	48520	Q2
22	HD 107369	0.37	0.02	1.1	2725.26	2568.38	2429.15	2705.92	7533 ± 250	2.45	$0.07^{+0.13}_{-0.05}$	910	814	1010	Q1
23	HD 112374	0.57	0.02	1.0	1763.78	1684.48	1619.4	1768.68	6393 ± 250	0.80	$0.30^{+0.10}_{-0.28}$	10777	9961	11882	Q1
24	HD 133656	0.56	0.03	0.9	1776.54	1707.63	1646.84	1781.63	8238 ± 250	1.38	$0.29^{+0.01}_{-0.08}$	5227	4861	5690	Q1
25	HR 6144	0.28	0.03	1.2	3561.19	3101.16	2894.87	3387.69	6728 ± 250	0.93	$0.11^{+0.15}_{-0.01}$	25491	22212	30419	Q1
26	HD 161796	0.5	0.02	1.2	1991.19	1920.96	1829.56	2015.66	6139 ± 250	0.99	$0.13^{+0.45}_{-0.13}$	5742	5209	6322	Q1
27	IRAS 18025−3906	0.54	0.19	8.6	1865.62	3046.67	1973.6	7194.98	6154 ± 250	1.18	$0.96^{+0.35}_{-0.17}$	2324	975	12963	Q2
28	HD 335675	0.03	0.18	13.7	30507.45	4888.53	3319.14	6540.55	6082 ± 250	1.58	$0.85^{+0.20}_{-0.04}$	15843	7303	28359	Q2
29	IRAS 19386+0155	0.32	0.16	11.6	3088.79	3631.35	2441.76	5588.81	6303 ± 250	1.00	$1.23^{+0.35}_{-0.14}$	9611	4345	22765	Q2
30	IRAS 19475+3119	0.32	0.02	1.4	3165.15	2971.43	2785.82	3135.57	8216 ± 250	1.01	$0.61^{+0.04}_{-0.16}$	6775	5955	7545	Q1
31	HR 7671	1.34	0.03	0.8	748.77	727.4	714.04	742.99	6985 ± 250	0.83	$0.40^{+0.11}_{-0.18}$	3579	3449	3734	Q1

Note. See Section 3 for more details.
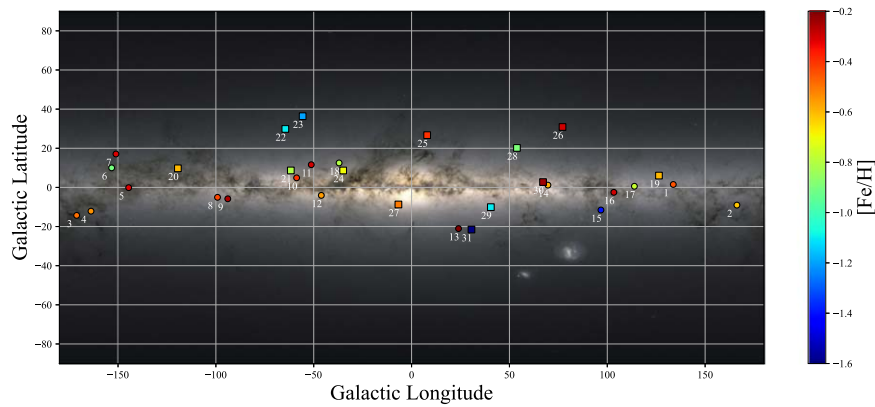
Figure 1. An edge-on Milky Way map with the positions of the sample stars marked. The filled-circle symbols represent the *s*-process enriched rich sources. The filled-square symbols represent the non-*s*-process enriched sources. The color bar represents the metallicity ([Fe/H]) of the objects.

Dominion Astrophysical Observatory in Victoria (Hrivnak et al. 2017). None of the objects have shown signatures of long-term variability in their radial velocity, thus confirming their likely single evolutionary nature. Therefore, we address the target sample as being all single stars.

3. Data Analysis: Total Reddening and Photospheric Luminosity Estimation

We use the latest available parallax data from the Gaia Early Data Release 3 (Gaia EDR3). We present the Gaia EDR3 identifiers and coordinates in Table 2 (see Appendix A). For the target sample, we obtained Gaia EDR3 parallaxes and their uncertainties, given with milliarcsecond accuracy (see Table 1). Table 1 also lists the distance obtained by inverting the parallax (i.e., $z_{(1/\mathrm{parallax})}$). However, it has been widely accepted that reliable distances cannot be obtained by inverting the parallax. To circumvent this issue, we use the distances from the study by Bailer-Jones et al. (2021), in which the authors adopt a probabilistic approach to estimating stellar distances. The approach involves the use of a prior constructed from a three-dimensional model of our galaxy, which includes interstellar extinction and Gaia's variable magnitude limit. In particular, we adopt the Bailer-Jones geometric distances (i.e., z_{BJ}; see Table 1). The geometric distances are derived from the Gaia EDR3 parallaxes with a direction-dependent prior on distance. We note that Bailer-Jones et al. (2021) also provides photogeometric distances that used the color and apparent magnitude of the individual stars by including assumptions that stars of a given color have a restricted range of probable absolute magnitudes (plus extinction). However, this assumption does not hold for post-AGB stars. We therefore use the Bailer-Jones geometric distances (i.e., z_{BJ}) and the associated upper and lower limits (z_{BJU} and z_{BJL}, respectively) in our further analysis. These values are tabulated in Table 1.

Based on the reliability of the Gaia EDR3 astrometric parameters (and hence the corresponding Bailer-Jones geometric distances, z_{BJ}), we categorize our target sample into two groups: Q1—high quality and Q2—low quality. We establish the quality flag (Q1 or Q2) based on the Gaia EDR3 renormalized unit weight error parameter (RUWE; see Lindegren et al. 2021), wherein RUWE $\gtrsim 1.4$ indicates likely unreliable astrometry. The RUWE parameters and the quality flags for the individual sources are listed in Table 1. Objects with high-RUWE objects could be partially resolved binary stars or tight astrometric binaries with a significant orbit-

induced displacement of the photocenter (Lindegren et al. 2021). However, this does not apply to our target sample because we address our target sample as being likely single stars or stars on very wide orbits and likely to evolve as single stars (see Section 2). Additionally, post-AGB objects can have a resolved nebula (e.g., Siódmiak et al. 2008; Lagadec et al. 2011; Ramos-Larios et al. 2012), which will impact the astrometric solution, resulting in a higher RUWE value. Therefore, while we consider both Q1 and Q2 objects in our data analysis, we only consider the Q1 objects while interpreting results and drawing conclusions (see Section 5).

To estimate the luminosity of the central star, i.e., the photospheric luminosity, we need to individually derive the total reddening, $E(B - V)$, which includes interstellar and circumstellar reddening, for all the sources. We do this by systematically constructing SEDs for all objects in our sample and minimizing the difference between the optical and near-IR fluxes and the reddened atmospheric models. The photometric data points for all objects are automatically retrieved from the Vizier database (Ochsenbein et al. 2000). For the atmospheric models, we used the appropriate Kurucz atmospheric models (Castelli & Kurucz 2003), the parameters of which were found in the spectroscopic analyses presented in previous studies (see the last column of Table 3). For the SED fitting, we interpolate in the chi-square (χ^2) region between the models centered around their spectroscopically determined parameters while also taking into account the uncertainty in the derived stellar parameters.

Figure 2 shows the example of one of the SEDs and the results from the fitting procedure. The SED fits for the full sample of objects are presented in Appendix B. We note that we assume that the total extinction in the line of sight has the wavelength dependency of the interstellar-medium extinction law (Cardelli et al. 1989) with $R_\mathrm{v} = 3.1$. It is probable that the circumstellar extinction law is different from the interstellar extinction law, but this exploration is beyond the scope of this study.

The uncertainty on the estimated total reddening parameter, $E(B - V)$, was computed by determining the confidence intervals of the free parameters. Subsequently, we determined the photospheric luminosity by integrating over all wavelengths the model atmosphere scaled, which we scaled to the dereddened photometric data. We note that stellar variability is not taken into account, and for high-amplitude variables, this translates into a higher χ^2 value. For objects with a high reddening value, the uncertainty on $E(B - V)$ can be significant (see Table 1). However, for the Q1 sources, the uncertainties on the $E(B - V)$
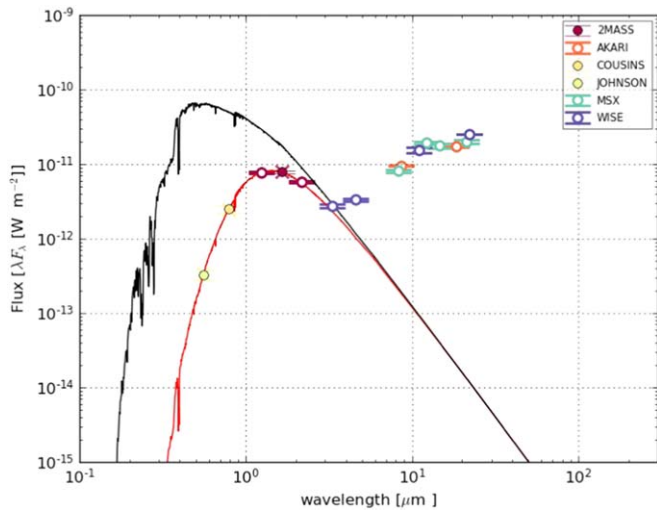
Figure 2. SED of the *s*-process enriched post-AGB object, IRAS Z02229 +6208 (see Table 1). The colored symbols represent the photometry of different passband filters, with the appropriate photometric catalog mentioned in the legend of the plot. The black solid line denotes the appropriate unreddened atmospheric model. The red line is the reddened model with $E(B - V) = 1.9$, fitted to the observed data. See text for more details.

values are small (see Table 1), and hence, the uncertainties on the luminosity are dominated by the uncertainties on the distances.

The derived luminosity ($L/L_\odot$) together with the upper and lower limits ($L_{\rm Upper}/L_\odot$ and $L_{\rm Lower}/L_\odot$), as well as the estimated $E(B - V)$, $T_{\rm eff}$, and $\log g$ of the best-fitting atmosphere model are tabulated in Table 1. $L_{\rm Upper}/L_\odot$ and $L_{\rm Lower}/L_\odot$ represent the impact of the uncertain distance (defined by $z_{\rm BJU}$, and $z_{\rm BJL}$) on the luminosity. While Table 1 lists the derived luminosities for all the objects in our target sample, we remind the reader that only the Q1 objects are with reliable astrometry and hence with reliable distances and derived luminosities. We anticipate that the upcoming Gaia DR3 data release (planned for 2022 June) will provide more reliable astrometry and the possibility to confirm the luminosities for the Q2 sources.

4. Positions of the Galactic Post-AGB Single Stars in the HR Diagram

4.1. Evolutionary Nature

To better understand the evolutionary stage of the target post-AGB objects with reliable Gaia DR3 astrometry and hence luminosities, we investigate the positions of the Q1 objects in the HR diagram (see Figure 3). For the sake of completeness, we also present the HR diagram with both Q1 and Q2 objects in Appendix C, but we do not further consider the Q2 objects.

In Figure 3, the *s*-process enriched Q1 objects are plotted as red filled circles, and the non-*s*-process enriched Q1 objects are plotted as blue filled squares. The effective temperatures ($T_{\rm eff}$) and photospheric luminosities ($L/L_\odot$) are those derived from the SED fitting explained above. Also shown in Figure 3 are the available evolutionary tracks of Miller Bertolami (2016) for post-AGB stars covering the final masses in the range 0.83–0.53 $M_\odot$. Because our target sample ranges from $-1.5 \lesssim {\rm [Fe/H]} \lesssim -0.3$ (see Table 2), we consider two different initial metallicities. The left panel of Figure 3 shows tracks with an initial metallicity of $Z = 0.001$ (i.e., ${\rm [Fe/H]} \approx -1.5$). The right panel of Figure 3 shows tracks with an initial metallicity of $Z = 0.01$ (i.e., ${\rm [Fe/H]} \approx -0.30$). Based on the positions of our Q1 targets on the HR diagram, we find that the majority of the objects sit within the final mass range of

0.53–0.83 $M_\odot$, which translates to the initial-mass range of $\sim$0.9–3.00 $M_\odot$, based on the empirically derived initial masses from the post-AGB evolutionary tracks of Miller Bertolami (2016).

We find that two non-*s*-process enriched stars (Object 19: IRAS 01259+6823 and Object 22: HD 107369) have luminosities <1000 $L_\odot$, suggesting that they never reached the AGB phase. These luminosities are significantly smaller than the typical luminosity of the tip of the red giant branch (RGB) (i.e., $\sim$2000–2500 $L_\odot$) and are similar to those of the dusty post-RGB stars (Kamath et al. 2016), which are the low-luminosity analogs of post-AGB objects. However, the dusty post-RGB stars are likely to be in binary systems, wherein the mass loss driven by the binary interaction prematurely terminated the RGB evolution, resulting in the objects evolving off the RGB as post-RGB objects. As explained in Section 2 the post-AGB stars are likely to be single objects.

A possibility is that these stars have completed their horizontal-branch (HB) evolution and are currently evolving through a post-HB phase that began after helium was exhausted in the core. The study by Greggio & Renzini (1990) showed that when the mass of the envelope above the helium core at the beginning of the HB phase is reduced to a few hundredths of a solar mass; the stars barely reach the AGB phase. Instead, after the HB evolution and a relatively short expansion phase, they start contracting, evolving through the so-called AGB-manqué phase (Greggio & Renzini 1990). According to this interpretation, such objects would be the counterparts of the stars populating the blue side of the HBs of some Galactic Globular Clusters, such as NGC 2419 (Ripepi et al. 2007) and NGC 2808 (Bedin et al. 2000). They descend from low-mass $M < 1\,M_\odot$ progenitors, thus they are likely to be the oldest objects in the sample.

Detailed evolutionary tracks of stars starting from the HB and extended until the start of the WD cooling track (for a range of masses between $\sim$0.5–0.6 $M_\odot$ and at appropriate initial metallicities) will be required to test whether these low-luminosity stars are indeed in the AGB-manqué phase. This is outside the scope of this observational paper but will be pursued in D. Kamath et al. (in preparation, hereafter referred to as Paper II).

4.2. Chemical Diversity

Interestingly, as shown in Figure 3, we find that there is no obvious separation in the luminosities (and hence current and initial masses) of the majority of the *s*-process enriched stars and the non-*s*-process enriched stars. This reveals that the observed bimodality in the *s*-process enrichment (see Section 1) is not purely a direct consequence of initial mass, as previously expected (Gallino et al. 1998; Karakas & Lugaro 2016). In Section 5 we further explore the chemical composition trends of the two classes of objects. We note that the current/initial mass is highly dependent on metallicity. In our subsequent study (Paper II), we are calculating dedicated stellar models, tailored to the appropriate stellar parameters of the individual objects, which will provide accurate current and initial-mass estimates and also allow for investigating the true nature of the individual objects based on their positions on the HR diagram as well as their observed chemical abundances.

5. Discussion and Conclusions

The derived luminosities for the Galactic Q1 post-AGB stars in our target sample together with their detailed surface compositions
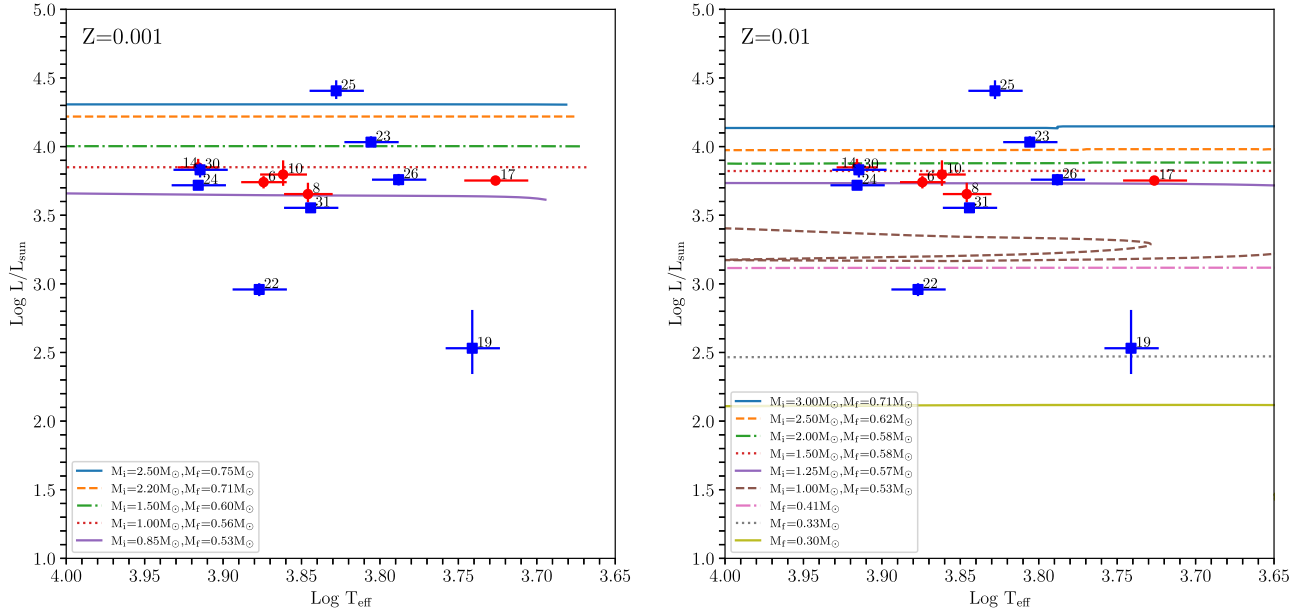
Figure 3. Positions of the Q1 post-AGB stars in the HR diagram. The red filled circles represent the *s*-process enriched objects and the blue filled squares represent the non-*s*-process enriched objects. The numbers represent the individual object numbers as listed in Table 1. Also shown are the available post-AGB evolutionary tracks of Miller Bertolami (2016) with $Z = 0.001$ (left panel) and $Z = 0.01$ (right panel). See text for more details.

have allowed us to confirm the evolutionary nature of these objects (via their positions in the HR diagram; see Figure 3) and draw important conclusions on the nucleosynthesis that occurred during and, to some extent, prior to the AGB phase.

The positions of the *s*-process enriched and non-*s*-process enriched stars in the HR diagram (Figure 3) have first confirmed that the majority of the objects in the target sample are indeed residing in the post-AGB phase of their lives. A small subset of objects (see Section 4) are likely to have had their evolution cut short and are likely to reside in the post-HB phase.

Additionally, as mentioned in Section 1, it was previously believed that the long-standing expectation that the *s*-process bimodality observed in single Galactic post-AGB stars is due to differences in their luminosities (and hence initial masses), with the *s*-process enriched population expected to be more luminous than the non-*s*-process0enriched population (Van Winckel 2003b). Our results show that there is no obvious distinction between the current luminosities (and hence current and initial masses) of the two populations.

To further investigate the two populations, we consider their metallicities and their derived abundance ratios of the CNO elements as a function of their *s*-process enrichment (see Table 2 in Appendix A). In Figure 4, we present the [Fe/H], [O/Fe], [C/Fe], and [N/Fe] ratios as a function of [s/Fe] for the target sample of post-AGB objects (see Figure 4). We maintain the same color-coding and symbols as before to represent the *s*-process enriched stars and the non-*s*-process enriched stars.

The top-left panel of Figure 4, which shows [Fe/H] versus [s/Fe] demonstrates that there is no obvious effect of [Fe/H] on the *s*-process bimodality. The objects from both groups show a spread in metallicity ranging from $-1.5 \lesssim$ [Fe/H] $\lesssim -0.3$. A similar conclusion can be drawn from the plot of the [O/Fe] versus [s/Fe] (top-right panel of Figure 4).

On the other hand, the plot showing [C/Fe] versus [s/Fe] (bottom-left panel of Figure 4) shows that, as expected from standard AGB nucleosynthesis theories (e.g., Fishlock et al. 2014; Karakas et al. 2018; Ventura et al. 2018), the majority of the *s*-process enriched population are more carbon-enhanced

(with [C/Fe] $\gtrsim 0.5$) while the non-*s*-process enriched population has [C/Fe] $\lesssim 0.5$.

The [N/Fe] versus [s/Fe] plot (bottom-right panel of Figure 4), which shows all the objects with available [N/Fe] ratios, reveals that for the *s*-process enriched population, the nitrogen enhancement is on average slightly lower compared to the non-*s*-process enriched population. By and large, based on Figures 3 and 4, it can be concluded that the population of stars showing *s*-process enrichment and the ones not showing *s*-process enhancements are mostly within the initial-mass range of 1–3 $M_\odot$ and with sub-solar metallicity.

We note that reliable astrometry will be required to investigate the Q2 objects and verify if the above conclusions drawn for the Q1 sample also apply to the Q2 sample.

We conclude that the *s*-process-rich and *s*-process non-enriched population of single Galactic post-AGB stars with reliable Gaia EDR3 astrometry covers the same metallicity range and luminosity distribution, revealing an intriguing chemical diversity observed among the sample of single post-AGB stars in the galaxy. We could not find observationally derived parameters that distinguish the two groups, apart from [C/Fe] and possibly [N/Fe]. The intriguing chemical diversity within a wide luminosity range shows that this is a fundamental shortcoming in our understanding of the chemical evolution of LIM stars. This suggests that the chemical evolution of LIM stars is not only dependent on the initial mass and metallicity but that additional parameters are needed to understand the diversity. Processes such as rotation (den Hartogh et al. 2019, e.g.), overshoot physics (e.g., Kamath et al. 2012; Goriely & Siess 2018), extra mixing (e.g., Karakas 2010; Karakas & Lattanzio 2014; Ventura et al. 2015), and mass loss (e.g., Cristallo et al. 2011; Karakas & Lattanzio 2014) can all affect the outcome of nucleosynthesis during and prior to the AGB phase. As the next step in our research, we will model all objects individually to investigate the parameter space needed to explain the chemical diversity in the luminosity range we probe. In Paper II, we will therefore first investigate, in detail, the CNO abundances of the individual objects. Subsequently, we will model the full *s*-process abundance
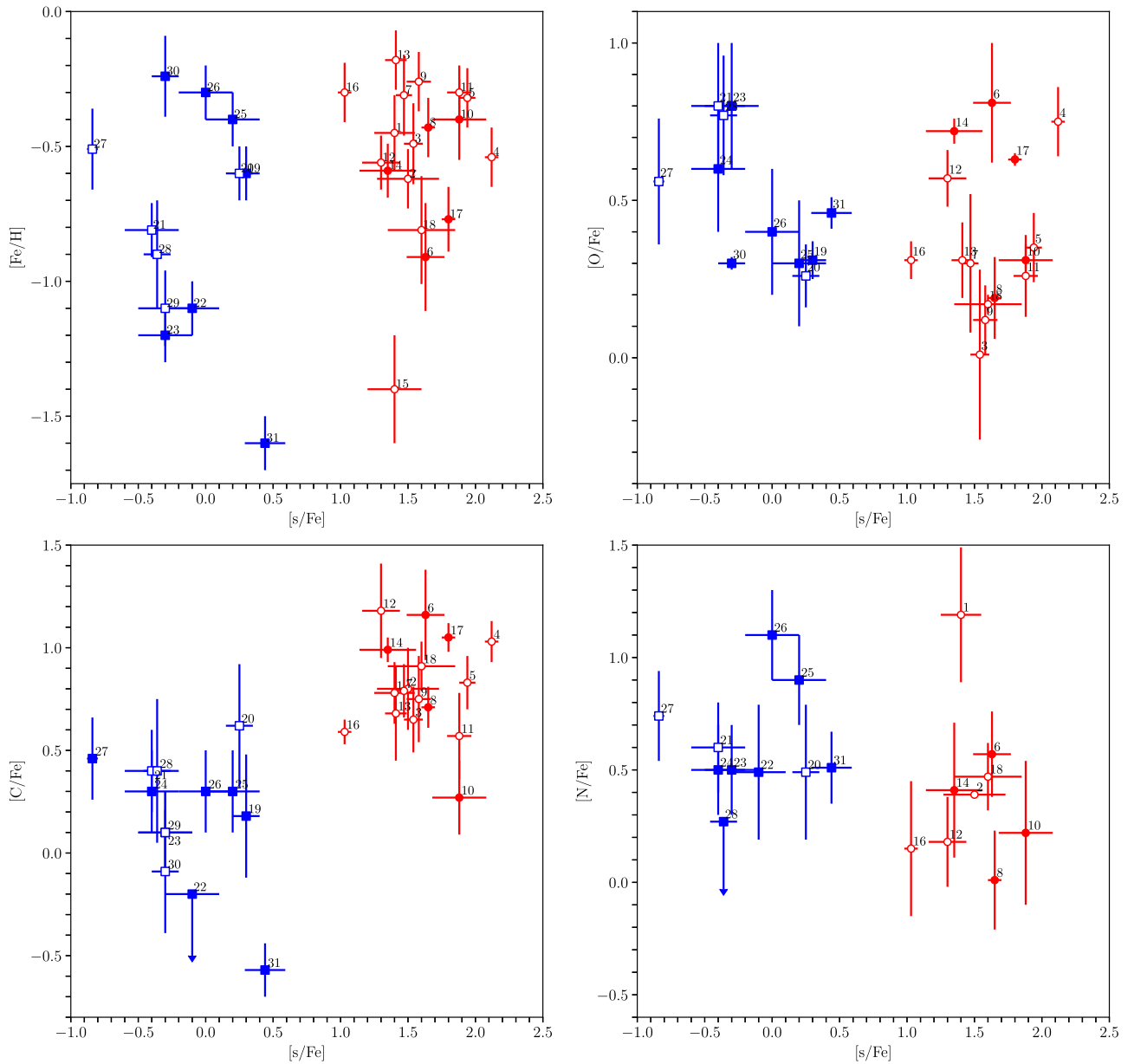
Figure 4. The [Fe/H] (top left), [O/Fe] (top right), [C/Fe] (bottom left), and [N/Fe] (bottom right) ratios as a function of [s/Fe] for the sample of post-AGB stars. The red circles represent the *s*-process enriched objects and the blue squares represent the non-*s*-process enriched objects. Filled symbols denote the Q1 objects, and the open symbols denote the Q2 objects. The numbers represent the individual object numbers as listed in Table 1. The derived abundances and errors are presented in Table 3. See Section 5 for more details.

profiles to gain insight into which parameters in the stellar evolution modeling are most deterministic in the *s*-process nucleosynthesis and photospheric enrichment processes.

Appendix A
Additional Target Details and the Chemical Abundances of the Sample

Here we present (see Table 2) additional information such as other names, the Gaia EDR3 identifier, and the coordinates of each of the individual objects. See Section 2 for more details. We also present the relevant chemical abundances (taken from literature) for each of the individual objects (see Table 3). See Section 5 for more details.

Table 2
A Compilation of the Various Names for the Target Sample Together with the Gaia EDR3 Identifiers, and the R.A. (°) and Decl. (°)

Index	IRAS Name	HR NAME	HD NAME	SAO Name	Other Names	Gaia EDR3 Identifier	R.A.(°)	Decl.(°)
					Post-AGB stars with *s*-process enrichment			
1	IRAS Z02229+6208	⋯	⋯	⋯	⋯	GAIA EDR3 513671461473684352	36.67411843	62.35611398
2	IRAS 04296+3429	⋯	⋯	⋯	GLMP 74	GAIA EDR3 173086700992466688	68.23740141	34.60344627
3	IRAS 05113+1347	⋯	⋯	⋯	GLMP 88	GAIA EDR3 3388902129107252992	78.53236845	13.84116291
4	IRAS 05341+0852	⋯	⋯	⋯	GLMP 106	GAIA EDR3 3334854780347915520	84.22938291	8.90240565
5	IRAS 06530−0213	⋯	⋯	⋯	GLMP 161, PN PM 1-24	GAIA EDR3 3105987960396950784	103.88258522	−2.29117496
6	IRAS 07134+1005	⋯	HD 56126	SAO 96709	V∗CY Cmi, BD+101470, GLMP 174	GAIA EDR3 3156171118495247360	109.04274454	9.99665253
7	IRAS 07430+1115	⋯	⋯	⋯	GLMP 192	GAIA EDR3 3151417586128916864	116.46415377	11.13875852
8	IRAS 08143−4406	⋯	⋯	⋯	GLMP 206, PN PM 1-39	GAIA EDR3 5520238967817034880	124.01257847	−44.26794331
9	IRAS 08281−4850	⋯	⋯	⋯	GLMP 218, PN PM 1-40	GAIA EDR3 5515266327706463616	127.41895483	−49.00119212
10	IRAS 12360−5740	⋯	⋯	⋯	GLMP 334	GAIA EDR3 6060828565581083264	189.72126697	−57.94218386
11	IRAS 13245−5036	⋯	⋯	⋯	GLMP 347	GAIA EDR3 6070128028770373888	201.90386260	−50.86837655
12	IRAS 14325−6428	⋯	⋯	⋯	⋯	GAIA EDR3 5849962851220246016	219.14313660	−64.69197718
13	IRAS 14429−4539	⋯	⋯	⋯	⋯	GAIA EDR3 5906408788891928704	298.21959045	−17.03065000
14	IRAS 19500−1709	⋯	HD 187885	SAO 163075	V∗ V5112 Sgr, BD-175779, GLMP 954	GAIA EDR3 6871175064823382912	300.49794561	32.79242099
15	IRAS 20000+3239	⋯	⋯	⋯	GLMP 963	GAIA EDR3 2034134414507432064	336.13092033	43.71970270
16	IRAS 22223+4327	⋯	⋯	⋯	V∗ V448 Lac, BD+424388, GLMP 1058	GAIA EDR3 1958757291756223104	337.29322799	54.85174583
17	IRAS 22272+5435	⋯	HD 235858	SAO 34504	V∗ V354 Lac, BD+542787, GLMP 1059	GAIA EDR3 2006425553228658816	353.18657229	62.06362764
18	IRAS 23304+6147	⋯	⋯	⋯	GLMP 1078	GAIA EDR3 2015785313459952128	221.55738007	−45.86812587
					Post-AGB stars without *s*-process enrichment			
19	IRAS 01259+6823	⋯	⋯	⋯	⋯	GAIA EDR3 532078488709487360	22.39034075	68.65402620
20	IRAS 08187−1905	⋯	HD 70379	⋯	V∗V552 Pup, BD-182290, GLMP 209	GAIA EDR3 5707613169577769600	125.23791728	−19.25094348
21	IRAS 12175−5338	⋯	⋯	SAO 239853	V∗V1024 Cen, GLMP 321	GAIA EDR3 6076326701687231872	185.06270566	−53.92538756
22	⋯	⋯	HD 107369	SAO 203367	⋯	GAIA EDR3 3469106382752903168	185.18720421	−32.55726017
23	IRAS 12538−2611	HR 4912	HD 112374	SAO 181244	V∗ LN Hya,	GAIA EDR3 3497154104039422848	194.12560314	−26.46038652
24	IRAS 15039−4806	⋯	HD 133656	SAO 225457	⋯	GAIA EDR3 5903310335089068416	226.86432907	−48.29833370
25	IRAS F16277−0724	HR 6144	HD 148743	SAO 141206	⋯	GAIA EDR3 4351018375858237952	247.62509302	−7.51444515
26	IRAS 17436+5003	⋯	HD 161796	SAO 30548	V∗V814 Her, BD+502457, GLMP 639	GAIA EDR3 1367102319545324288	266.23111123	50.04424810
27	IRAS 18025-3906	⋯	⋯	⋯	GLMP 713	GAIA EDR3 4035907203854415488	271.51374773	−39.09910702
28	IRAS 18095+2704	⋯	HD 335675	⋯	V∗ V887 Her, GLMP 735	GAIA EDR3 4580154606223711872	272.87773398	27.08767172
29	IRAS 19386+0155	⋯	⋯	⋯	V∗V1648 Aql	GAIA EDR3 4240112390324832384	295.28454494	2.04197942
30	IRAS 19475+3119	⋯	HD 331319	⋯	V∗V2513 Cyg, BD+313797, GLMP 951	GAIA EDR3 2033763428091006720	297.37317348	31.45450606
31	IRAS 20023−1144	HR 7671	HD 190390	SAO 163245	V∗V1401 Aql, BD-125641	GAIA EDR3 4190636669164572928	301.27254423	−11.59948519

Table 3
Chemical Abundances of the *s*-process Enriched and Non-*s*-process Enriched Single Galactic Post-AGB stars

Index	Object Name	[Fe/H]	[C/O]	[O/Fe]	[C/Fe]	[N/Fe]	[Zr/Fe]	[s/Fe]	[ls/Fe]	[hs/Fe]	[hs/ls]	Reference
					Post-AGB stars with *s*-process enrichment							
1	IRAS Z02229+6208	−0.45 ± 0.14	⋯	⋯	0.78 ± 0.15	1.19 ± 0.30	2.22 ± 0.13	1.4 ± 0.15	2.03 ± 0.12	1.12 ± 0.03	−0.91 ± 0.12	1
2	IRAS 04296+3429	−0.62 ± 0.11	⋯	⋯	0.8 ± 0.2	0.39 ± 0.01	1.34 ± 0.23	1.5 ± 0.23	1.7 ± 0.23	1.5 ± 0.17	−0.2 ± 0.23	2
3	IRAS 05113+1347	−0.49 ± 0.15	2.42 ± 0.40	0.01 ± 0.27	0.65 ± 0.16	⋯	1.36 ± 0.15	1.54 ± 0.07	1.33 ± 0.13	1.65 ± 0.07	0.32 ± 0.15	3
4	IRAS 05341+0852	−0.54 ± 0.11	1.06 ± 0.30	0.75 ± 0.11	1.03 ± 0.10	⋯	1.76 ± 0.10	2.12 ± 0.05	1.87 ± 0.08	2.24 ± 0.06	0.37 ± 0.10	3
5	IRAS 06530−0213	−0.32 ± 0.11	1.66 ± 0.39	0.35 ± 0.11	0.83 ± 0.13	⋯	1.60 ± 0.10	1.94 ± 0.06	1.75 ± 0.09	2.04 ± 0.08	0.29 ± 0.13	3
6	IRAS 07134+1005	−0.91 ± 0.20	1.24 ± 0.29	0.81 ± 0.19	1.16 ± 0.22	0.57 ± 0.19	1.61 ± 0.09	1.63 ± 0.14	1.64 ± 0.13	1.63 ± 0.20	−0.01 ± 0.24	3
7	IRAS 07430+1115	−0.31 ± 0.15	1.71 ± 0.30	0.30 ± 0.22	0.79 ± 0.13	⋯	1.22 ± 0.15	1.47 ± 0.06	1.30 ± 0.14	1.55 ± 0.06	0.25 ± 0.15	3
8	IRAS 08143−4406	−0.43 ± 0.11	1.66 ± 0.39	0.19 ± 0.13	0.71 ± 0.10	0.01 ± 0.22	1.63 ± 0.11	1.65 ± 0.05	1.77 ± 0.08	1.58 ± 0.06	−0.19 ± 0.11	3
9	IRAS 08281−4850	−0.26 ± 0.11	2.34 ± 0.42	0.12 ± 0.11	0.75 ± 0.21	⋯	1.42 ± 0.11	1.58 ± 0.09	1.57 ± 0.11	1.58 ± 0.12	0.01 ± 0.17	3
10	IRAS 12360−5740	−0.40 ± 0.15	0.45 ± 0.20	0.31 ± 0.05	0.27 ± 0.18	0.22 ± 0.32	1.70 ± 0.17	1.88 ± 0.20	1.73 ± 0.20	2.02 ± 0.20	0.29 ± 0.20	4
11	IRAS 13245−5036	−0.30 ± 0.10	1.11 ± 0.30	0.26 ± 0.13	0.57 ± 0.21	⋯	1.72 ± 0.15	1.88 ± 0.09	1.56 ± 0.14	2.03 ± 0.11	0.47 ± 0.18	3
12	IRAS 14325−6428	−0.56 ± 0.10	2.27 ± 0.40	0.57 ± 0.09	1.18 ± 0.23	0.18 ± 0.20	1.16 ± 0.16	1.30 ± 0.14	1.25 ± 0.15	1.33 ± 0.19	0.08 ± 0.24	3
13	IRAS 14429−4539	−0.18 ± 0.11	1.29 ± 0.26	0.31 ± 0.12	0.68 ± 0.23	⋯	1.46 ± 0.17	1.41 ± 0.08	1.29 ± 0.15	1.47 ± 0.10	0.18 ± 0.08	3
14	IRAS 19500−1709	−0.59 ± 0.10	1.02 ± 0.17	0.72 ± 0.04	0.99 ± 0.06	0.41 ± 0.30	1.34 ± 0.10	1.35 ± 0.21	1.37 ± 0.29	1.34 ± 0.30	−0.03 ± 0.41	3
15	IRAS 20000+3239	−1.4 ± 0.2	⋯	⋯	1.7 ± 0.2	2.1 ± 0.2	1 ± 0.2	1.4 ± 0.2	1.1 ± 0.2	1.47 ± 0.10	0.34 ± 0.2	5
16	IRAS 22223+4327	−0.30 ± 0.11	1.04 ± 0.22	0.31 ± 0.06	0.59 ± 0.06	0.15 ± 0.30	1.35 ± 0.06	1.03 ± 0.05	1.34 ± 0.07	0.88 ± 0.07	−0.46 ± 0.10	3
17	IRAS 22272+5435	−0.77 ± 0.12	1.46 ± 0.26	0.63 ± 0.02	1.05 ± 0.07	⋯	1.54 ± 0.08	1.80 ± 0.05	1.61 ± 0.08	1.90 ± 0.07	0.28 ± 0.11	3
18	IRAS 23304+6147	−0.81 ± 0.2	2.8 ± 0.2	0.17 ± 0.03	0.91 ± 0.12	0.47 ± 0.15	1.26 ± 0.23	1.60 ± 0.25	1.55 ± 0.23	1.63 ± 0.21	0.09 ± 0.24	6
					Post-AGB stars without *s*-process enrichment							
19	IRAS 01259+6823	−0.60 ± 0.1	0.4 ± 0.3	0.31 ± 0.06	0.18 ± 0.3	⋯	0.12 ± 0.1	0.3 ± 0.1	⋯	⋯	⋯	7
20	IRAS 08187−1905	−0.60 ± 0.1	⋯	0.26 ± 0.1	0.62 ± 0.3	0.49 ± 0.3	0.25 ± 0.1	⋯	⋯	⋯	⋯	7
21	SAO 239853	−0.81 ± 0.1	⋯	0.8 ± 0.2	0.4 ± 0.2	0.6 ± 0.2	⋯	−0.4 ± 0.2	⋯	⋯	⋯	8
22	HD 107369	−1.1 ± 0.1	⋯	0 ± 0.2	<−0.2	0.49 ± 0.3	⋯	−0.1 ± 0.2	⋯	⋯	⋯	8
23	HD 112374	−1.2 ± 0.1	⋯	0.8 ± 0.2	0.1 ± 0.2	0.5 ± 0.2	⋯	−0.3 ± 0.2	⋯	⋯	⋯	8
24	HD 133656	−0.7 ± 0.1	⋯	0.6 ± 0.2	0.3 ± 0.2	0.5 ± 0.2	⋯	−0.4 ± 0.2	⋯	⋯	⋯	8
25	HR 6144	−0.4 ± 0.1	⋯	0.3 ± 0.2	0.3 ± 0.2	0.9 ± 0.2	⋯	0.2 ± 0.2	⋯	⋯	⋯	8
26	HD 161796	−0.3 ± 0.1	⋯	0.4 ± 0.2	0.3 ± 0.2	1.1 ± 0.2	⋯	0 ± 0.2	⋯	⋯	⋯	8
27	IRAS 18025-3906	−0.51 ± 0.15	0.43	0.56 ± 0.2	0.46 ± 0.2	0.74 ± 0.2	−0.84 ± 0.04	⋯	⋯	⋯	⋯	9
28	HD 335675	−0.9 ± 0.2	0.25	0.77–0.19	0.4–0.35	<0.27	−0.36 ± 0.1	⋯	⋯	⋯	⋯	10
29	IRAS 19386+0155	−1.1 ± 0.14	⋯	⋯	0.1 ± 0.2	⋯	⋯	−0.3 ± 0.2	⋯	⋯	⋯	11
30	IRAS 19475+3119	−0.24 ± 0.15	0.19	0.30 ± 0.02	−0.09 ± 0.30	⋯	⋯	−0.30 ± 0.1	⋯	⋯	⋯	12
31	HR 7671	−1.6 ± 0.1	0.05	0.46 ± 0.05	−0.57 ± 0.13	0.51 ± 0.16	0.44 ± 0.15	⋯	⋯	⋯	⋯	13

Note. The index [s/Fe] is the mean of the relative abundances of the elements for the "ls" and "hs" indices. Typically, 'ls' refers to the light *s*-process elements, which in this case is represented by the relative abundances of Y and Zr, and 'hs' refers to the heavy s-process elements, which in this case is represented by the relative abundances of La, Ce, Nd, and Sm. [hs/ls] = [hs/Fe] − [ls/Fe]. More details on the derived abundances and abundance ratios can be found in the individual studies mentioned in column "Ref". The column "Ref." indicates the individual chemical abundance study: (1) Reddy et al. (1999), (2) Van Winckel & Reyniers (2000), (3) De Smedt et al. (2016), (4) Pereira et al. (2011), (5) Klochkova & Kipper (2006), (6) Reyniers (2000), (7) Rao et al. (2012), (8) Van Winckel (1997), (9) Molina et al. (2019), (10) Şahin et al. (2011), (11) Pereira et al. (2004), (12) Arellano Ferro et al. (2001), (13) Reyniers & Cuypers (2005).

Appendix B
Spectral Energy Distributions (SEDs)

In this appendix, we show the SEDs of the target sample of post-AGB stars (Q1 and Q2 objects, see Figures 5–7). See Section 3 for full details on the SED fitting. With regard to the photometric data points, as mentioned in Section 3, we queried the photometry from the Vizier database (Ochsenbein et al. 2000). We refer to Appendix A of Oomen et al. (2018) for the individual photometric catalogs used.
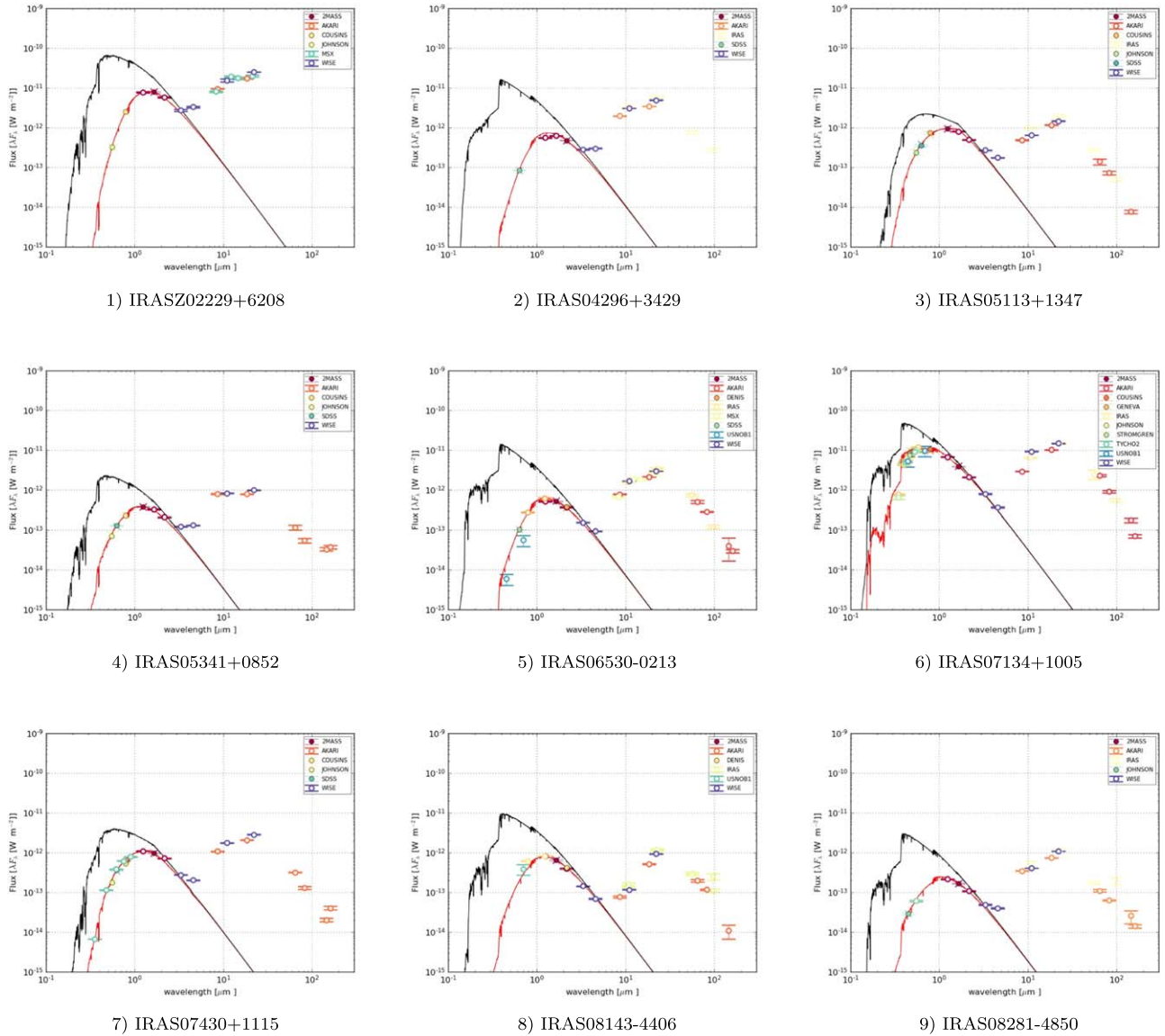

Figure 5. List of all SEDs of the post-AGB stars in our target sample. The order of the objects is the same as that in Table 1. The black curve represents the atmospheric model. Details of the atmosphere model (e.g., T_{eff}, and $E(B-V)$ are listed in Table 1. The red solid curve is the reddened atmospheric model (see Section 3 for more details). The various symbols correspond to the observed photometric data points where different colors denote the different surveys mentioned on the plot.
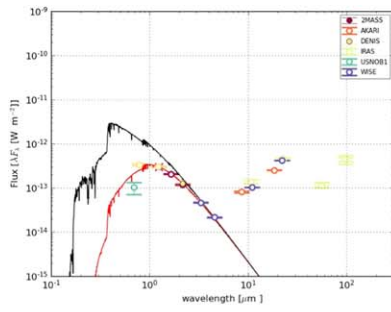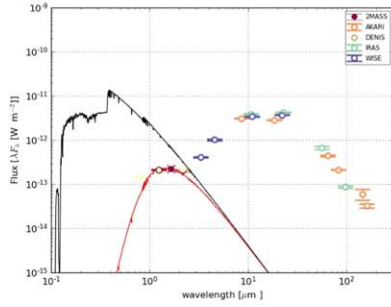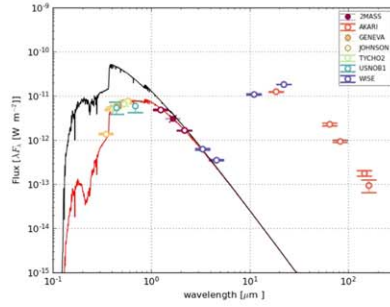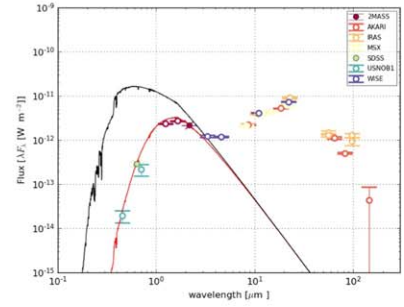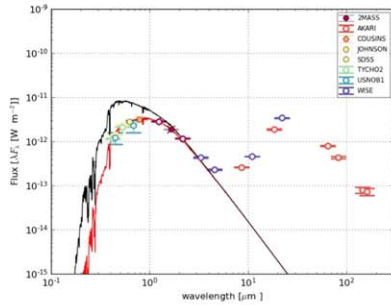
10) IRAS12360-5740
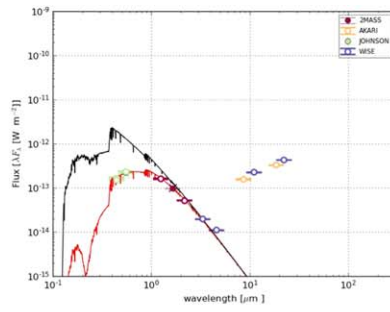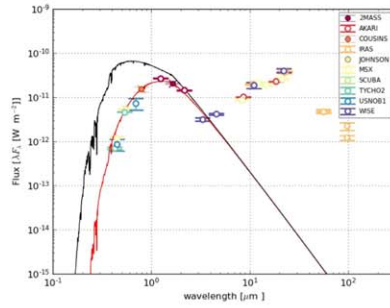
11) IRAS13245-5036
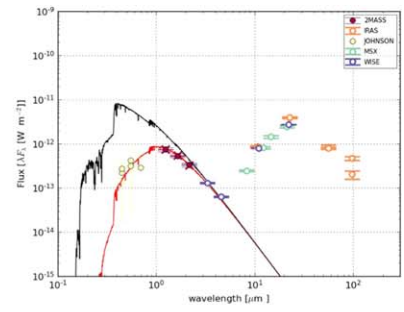
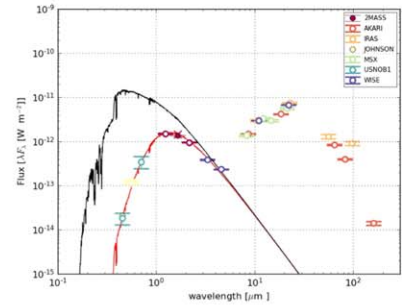12) IRAS14325-6428

13) IRAS14429-4539
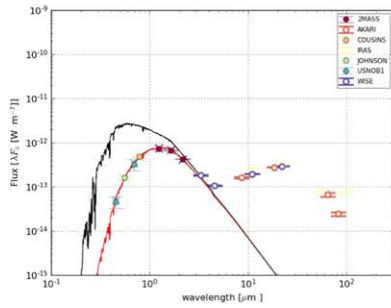
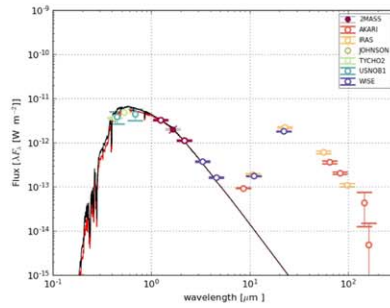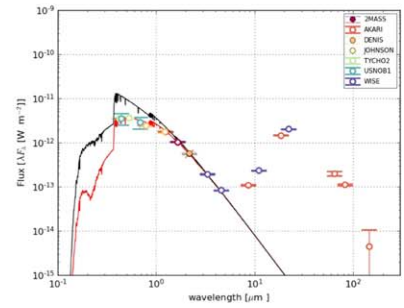14) IRAS19500-1709

15) IRAS20000+3239

16) IRAS22223+4327

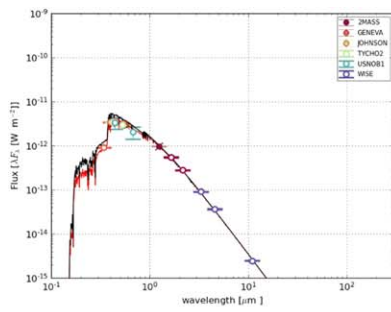17) IRAS22272+5435

18) IRAS23304+6147
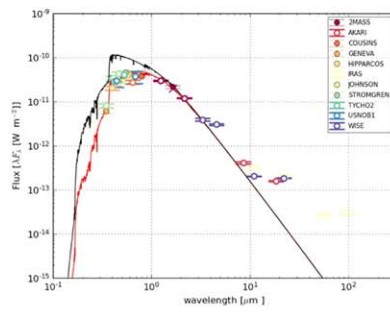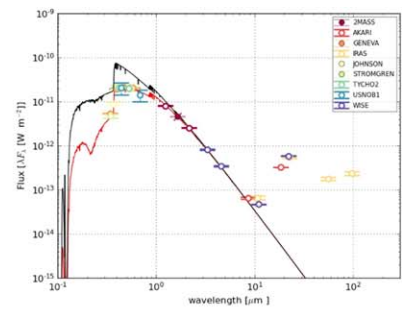
19) IRAS01259+6823

20) IRAS08187-1905

21) SAO239853

Figure 6. Figure 5 continued.

22) HD107369

23) HD112374

24) HD133656
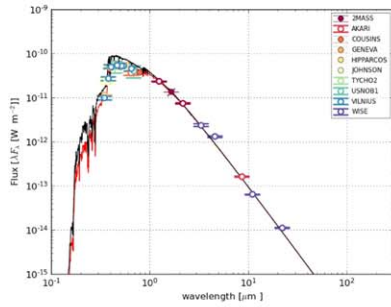
25) HR6144
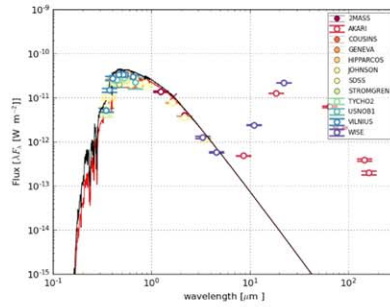
26) HD161796
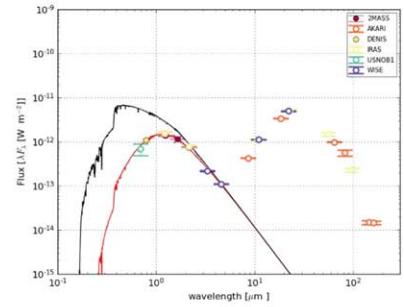
27) IRAS18025-3906
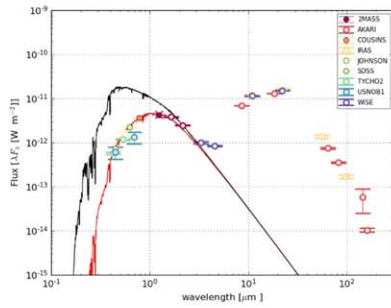
28) IRAS18095+2704
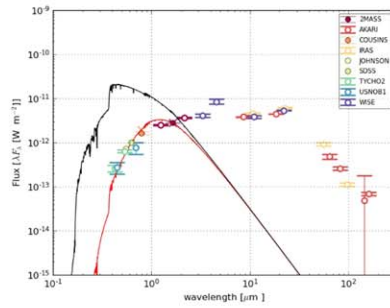
29) IRAS19386+0155
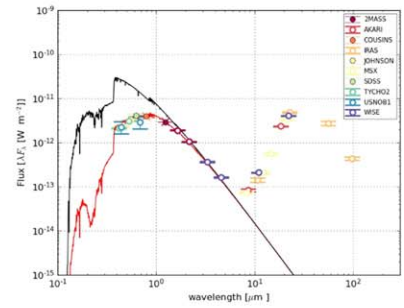
30) IRAS19475+3119
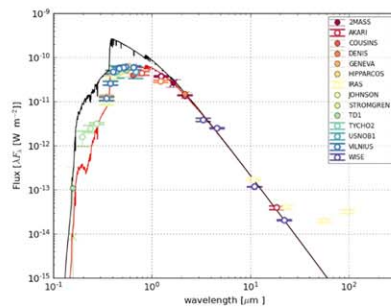
31) HR7671

Figure 7. Figure 5 continued.

Appendix C
Positions of the Q1 and Q2 Galactic Post-AGB Single Stars in the HR Diagram

In this appendix, we present Figure 8, which shows the positions of the Q1 and Q2 Galactic post-AGB single stars in the HR diagram. See Section 4.1 for further details.

Figure 8. Positions of the Q1 and Q2 post-AGB stars in the HR diagram. The red filled circles represent the *s*-process enriched Q1 objects and the blue filled squares represent the non-*s*-process enriched Q1 objects. The red open circles represent the *s*-process enriched Q2 objects and the blue open squar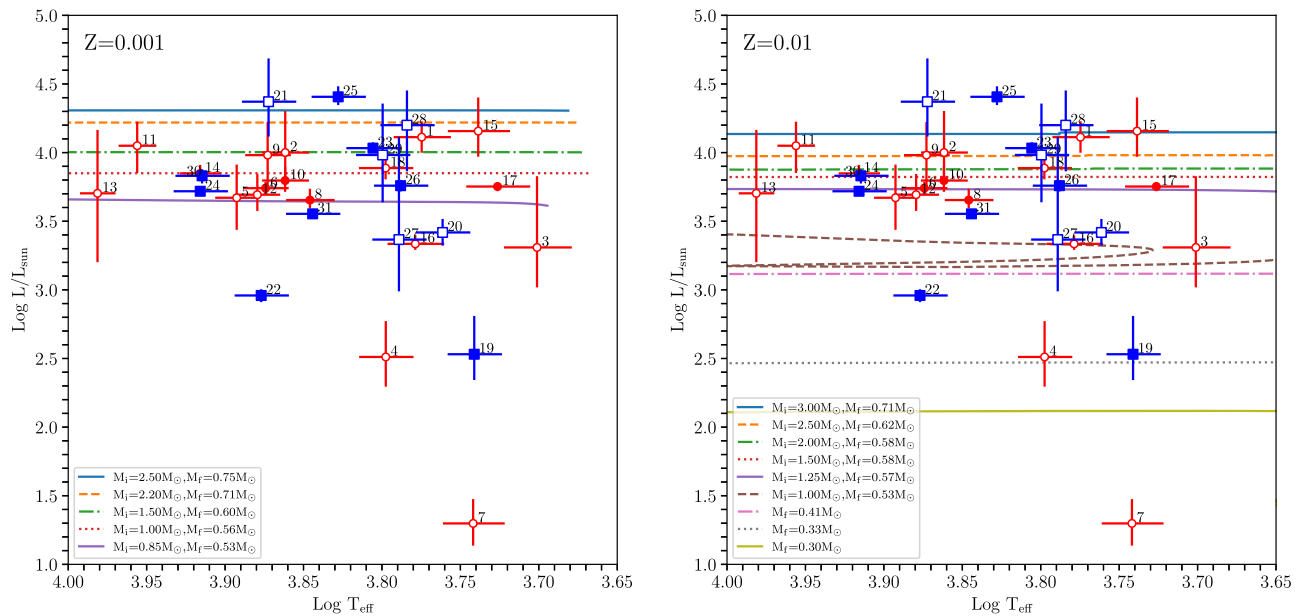es represent the non-*s*-process enriched Q2 objects. The numbers represent the individual object numbers as listed in Table 1. Also shown are the available post-AGB evolutionary tracks of Miller Bertolami (2016) with $Z = 0.001$ (left panel) and $Z = 0.01$ (right panel). See text for more details.

ORCID iDs

Devika Kamath ● https://orcid.org/0000-0001-8299-3402
Hans Van Winckel ● https://orcid.org/0000-0001-5158-9327
Paolo Ventura ● https://orcid.org/0000-0002-5026-6400
Maksym Mohorian ● https://orcid.org/0000-0002-7453-294
Bruce J. Hrivnak ● https://orcid.org/0000-0003-1471-8892
Flavia Dell'Agli ● https://orcid.org/0000-0003-2442-6981
Amanda Karakas ● https://orcid.org/0000-0002-3625-6951

References

Abia, C., de Laverny, P., & Wahlin, R. 2008, A&A, 481, 161
Arellano Ferro, A., Giridhar, S., & Mathias, P. 2001, A&A, 368, 250
Bailer-Jones, C. A. L., Rybizki, J., Fouesneau, M., Demleitner, M., & Andrae, R. 2021, AJ, 161, 147B
Bedin, L. R., Piotto, G., Zoccali, M., et al. 2000, A&A, 363, 159
Cardelli, J. A., Clayton, G. C., & Mathis, J. S. 1989, ApJ, 345, 245
Castelli, F., & Kurucz, R. L. 2003, in IAU Symp. 210, Modelling of Stellar Atmospheres 210, ed. N. Piskunov, W. W. Weiss, & D. F. Gray (San Francisco, CA: ASP), A20
Cristallo, S., Piersanti, L., Straniero, O., et al. 2011, ApJS, 197, 17
Şahin, T., Lambert, D. L., Klochkova, V. G., & Tavolganskaya, N. S. 2011, MNRAS, 410, 612
De Smedt, K., Van Winckel, H., Kamath, D., et al. 2016, A&A, 587, A6
De Smedt, K., Van Winckel, H., Karakas, A. I., et al. 2012, A&A, 541, A67
den Hartogh, J. W., Hirschi, R., Lugaro, M., et al. 2019, A&A, 629, A123
Fishlock, C. K., Karakas, A. I., Lugaro, M., & Yong, D. 2014, ApJ, 797, 44
Gallino, R., Arlandini, C., Busso, M., et al. 1998, ApJ, 497, 388
García-Hernández, D. A., García-Lario, P., Plez, B., et al. 2007, A&A, 462, 711
Giridhar, S., & Arellano Ferro, A. 2005, A&A, 443, 297
Goriely, S., & Siess, L. 2018, A&A, 609, A29
Greggio, L., & Renzini, A. 1990, ApJ, 364, 35
Hinkle, K. H., Lebzelter, T., & Straniero, O. 2016, ApJ, 825, 38
Hrivnak, B. J., Henson, G., Hillwig, T. C., et al. 2021, AJ, 162, 248
Hrivnak, B. J., Lu, W., Maupin, R. E., & Spitzbart, B. D. 2010, ApJ, 709, 1042
Hrivnak, B. J., Lu, W., & Nault, K. A. 2015, AJ, 149, 184

Hrivnak, B. J., Van de Steene, G., Van Winckel, H., et al. 2017, ApJ, 846, 96
Kamath, D. 2020, JApA, 41, 42
Kamath, D., Karakas, A. I., & Wood, P. R. 2012, ApJ, 746, 20
Kamath, D., & Van Winckel, H. 2019, MNRAS, 486, 3524
Kamath, D., Van Winckel, H., Wood, P. R., et al. 2017, ApJ, 836, 15
Kamath, D., Wood, P. R., & Van Winckel, H. 2014, MNRAS, 439, 2211
Kamath, D., Wood, P. R., & Van Winckel, H. 2015, MNRAS, 454, 1468
Kamath, D., Wood, P. R., Van Winckel, H., & Nie, J. D. 2016, A&A, 586, L5
Karakas, A. I. 2010, MNRAS, 403, 1413
Karakas, A. I., & Lattanzio, J. C. 2014, PASA, 31, e030
Karakas, A. I., & Lugaro, M. 2016, ApJ, 825, 26
Karakas, A. I., Lugaro, M., Carlos, M., et al. 2018, MNRAS, 477, 421
Klochkova, V. G., & Kipper, T. 2006, BaltA, 15, 395
Kobayashi, C., Karakas, A. I., & Lugaro, M. 2020, ApJ, 900, 179
Kwok, S., Boreiko, R. T., & Hrivnak, B. J. 1987, ApJ, 312, 303
Lagadec, E., Verhoelst, T., Mékarnia, D., et al. 2011, MNRAS, 417, 32
Lindegren, L., Klioner, S. A., Hernández, J., et al. 2021, A&A, 649, A2
Miller Bertolami, M. M. 2016, A&A, 588, A25
Molina, R. E., Pereira, C. B., & Arellano Ferro, A. 2019, arXiv:1901.05866
Nie, J. D., Wood, P. R., & Nicholls, C. P. 2012, MNRAS, 423, 2764
Ochsenbein, F., Bauer, P., & Marcout, J. 2000, A&AS, 143, 23
Oomen, G.-M., Van Winckel, H., Pols, O., et al. 2018, A&A, 620, A85
Pereira, C. B., Lorenz-Martins, S., & Machado, M. 2004, A&A, 422, 637
Pereira, C. B., Sales Silva, J. V., Chavero, C., Roig, F., & Jilinski, E. 2011, A&A, 533, A51
Pérez-Mesa, V., Zamora, O., García-Hernández, D. A., et al. 2019, A&A, 623, A151
Ramos-Larios, G., Guerrero, M. A., Suárez, O., Miranda, L. F., & Gómez, J. F. 2012, A&A, 545, A20
Rao, S. S., Giridhar, S., & Lambert, D. L. 2012, MNRAS, 419, 1254
Raskin, G., van Winckel, H., Hensberge, H., et al. 2011, A&A, 526, A69
Reddy, B. E., Bakker, E. J., & Hrivnak, B. J. 1999, ApJ, 524, 831
Reyniers, M. 2000, PhD thesis, Institute of Astronomy, KU Leuven
Reyniers, M., & Cuypers, J. 2005, A&A, 432, 595
Ripepi, V., Clementini, G., Di Criscienzo, M., et al. 2007, ApJL, 667, L61
Siódmiak, N., Meixner, M., Ueta, T., et al. 2008, ApJ, 677, 382
Sloan, G. C., Kraemer, K. E., Wood, P. R., et al. 2008, ApJ, 686, 1056
Szczerba, R., Siódmiak, N., Stasińska, G., & Borkowski, J. 2007, A&A, 469, 799
van Aarle, E., Van Winckel, H., Lloyd Evans, T., et al. 2011, A&A, 530, A90

Van Winckel, H. 1997, A&A, 319, 561

Van Winckel, H. 2003a, ARA&A, 41, 391

Van Winckel, H. 2003b, in IAU Symp. 209, Planetary Nebulae: Their Evolution and Role in the Universe, ed. S. Kwok, M. Dopita, & R. Sutherland (San Francisco, CA: ASP), 91

van Winckel, H. 2017, in IAU Symposium, Vol. 323, Planetary Nebulae: Multi-Wavelength Probes of Stellar and Galactic Evolution (San Francisco, CA: ASP), 231

Van Winckel, H., Lloyd Evans, T., Briquet, M., et al. 2009, A&A, 505, 1221

Van Winckel, H., & Reyniers, M. 2000, A&A, 354, 135

Vassiliadis, E., & Wood, P. R. 1993, ApJ, 413, 641

Ventura, P., Karakas, A., Dell'Agli, F., García-Hernández, D. A., & Guzman-Ramirez, L. 2018, MNRAS, 475, 2282

Ventura, P., Karakas, A. I., Dell'Agli, F., et al. 2015, MNRAS, 450, 3181